Micro-Scale Deformation of Gypsum during Micro-Indentation Loading

James D. Hogan[a,b], Suporn Boonsue[b], John G. Spray[b], Robert J. Rogers[a]

[a]*Department of Mechanical Engineering, University of New Brunswick, Fredericton, New Brunswick E3B 5A3, Canada*
[b]*Planetary and Space Science Centre, University of New Brunswick, Fredericton, New Brunswick E3B 5A3, Canada*

Abstract

Micro-scale deformation and fracture of a gypsum crystal under micro-indentation loading was examined. Results indicate that the hardness decreases with increasing load, on all axes, ranging from 216 kg/mm^2 at 0.25 N to 91 kg/mm^2 at 4.91 N on the (010) axis and from 122 kg/mm^2 at 0.98 N to 75 kg/mm^2 at 4.91 N on the (011) and (110) preferred cleavage planes. Higher hardness values for lower loads are attributed to dislocation saturation and localized necking which leads to work-hardening and densification. Transmitted light microscopy revealed the decrease in hardness for increasing load was related to an increase in subsurface cracking along the (010) and (011) cleavage planes, enabling the indenter to penetrate deeper into the crystal. Coupled with the increase in subsurface cracking was an increase in surface smoothness as a result of increased plastic material flow beneath the indenter, with surface dislocation densities decreasing from 34 $\%$ at a 0.25 N load to 6 $\%$ at a 4.91 N loading. Raman spectroscopy revealed that this material was mainly comprised of water-reduced forms of gypsum: hemihydrate

Email address: jd.hogan@unb.ca (James D. Hogan)

and γ-$CaSO_4$. Local temperatures required for the dehydration of gypsum range from 118 to 142°C [1], indicating such temperatures are reached during plastic flow, and related heat generation, of the material beneath the indenter. Evaporated water leaves behind voids in the crystal structure and enables the gypsum to deform more easily.

Keywords: microscale deformation and fracture, Vickers testing, gypsum dehydration, mineral processing, rock mechanics, scanning electron microscopy

---

1. Introduction

Understanding deformation and fracture mechanisms [2–5] in rocks and minerals is important in planetary science [6], blasting and mining industries [7], in military and shielding applications [8, 9], and in manufacturing industries [10]. Fracture mechanisms can take many forms depending on scale; with the bulk of the research being performed at scales $>$100 μm. Micro-scale deformation and fracture mechanisms have received less attention despite their importance in machining (e.g., sawing [11], drilling [12], grinding [13]), in abrasion and wear applications [14, 15], and in comminution [16] and fragmentation [4]. Here we report on the investigation of micro-scale deformation and fracture mechanisms in gypsum crystals.

Gypsum is a soft, monoclinic mineral (Mohs hardness of 2 and Vickers hardness of approximately 60 kg/mm^2 [17, 18]) with a specific gravity of 2.31. It is composed of calcium sulfate dihydrate, with the chemical formula $CaSO_4{\cdot}2H_20$. Gypsum is primarily used in finish boards for walls and ceilings (drywall), and in plaster of Paris used in surgical splints and dental materials [19]. Gypsum is moderately water-soluble ($\sim$ 2.0-2.5 g/L at 25°C) and gypsum crystals are

found to contain anion water, making it an important indicator of water in ancient evaporitic lake beds on, for example, Mars [20]. Experimenting on single crystals is important for engineering applications and in material science research as crystal structure and orientation are closely related to strength properties of the mineral [21]. Further, deformation and fracture characteristics are simplified and measurements are more repeatable for single-crystal measurements [22], enabling a more detailed understanding of the mineral's behaviour under controlled experimental conditions.

The experimental study of the behaviour of rock and mineral deformation is typically accomplished using conventional methods, such as split Hokpinson-bar testing [23], tensile and compression testing [24, 25], through rebound tests (e.g., the Shore Scleroscope [26], the Schmidt Hammer [27]), and Charpy notch testing [28]. Impact testing [9, 29, 30] and various machining techniques, including sawing [11], drilling [12], and cutting using a waterjet [31], have also been developed to study deformation and fracture mechanisms. Of particular interest, and used here to study the micro-scale deformation of a gypsum crystal, is the microhardness indentation technique.

Microhardness tests have been a benchmark method for determining the hardness and fracture characteristics of brittle materials [32, 33]. These can be used to model sawing and grinding scenarios, as well as abrasion and wear applications. Exploring deformation and fracture mechanisms using microhardness measurements has been undertaken in many different materials since early works by Tabor [17] and Mott [34]. For example, limestone [22], marble [22], anhydrite [22], artificial rock salt [22, 35], soda-lime glass [33, 36], TiC crystals [37], olivine [38], and quartz [38, 39] have all been studied using a form of microhardness testing.

Microhardness indentation techniques offer many advantages over more conventional test arrangements, including: economy in material and time, reproducibility of results, simplicity in experimentation, capacity to survey an inhomogeneous surface for micro-strength variations and residual stresses, and sampling bulk and single grain properties. The objective of the present study is to investigate the response of gypsum crystals under micro-indentation loading. Micro-scale deformation and fracture mechanisms are characterized using transmitted light micrscopy and field emission scanning electron microscope. Raman spectroscopy is used to determine phase transformations.

2. Experimental Setup

Vickers microhardness experiments on a single gypsum crystal were performed at the University of New Brunswick using a Leitz Vickers tester under a 17 second loading cycle. A photograph of the gypsum crystals and corresponding principal axes definitions are shown in Figure 1. In the Vickers microhardness test, a diamond pyramid (136° apical angle) is pressed under known load into a flat surface. A pyramid indenter is preferable over spherical indenters because of the symmetry of the residual stress field left by the indenter when the load is removed [17]. The indentation results in a complex stress field [22], which promotes a variety of irreversible deformation modes such as plastic flow, structural densification [33], and ensuing microfracturing, both at the surface [22, 33] (as median and radial cracking) and below the indenter as Hertzian (lateral) cracking [40–43]. Loads of 0.25 N to 4.91 N (25 g to 500 g) were applied at room temperature on the (010), (110) and (011) axes (red circles in Figure 1).

Experiments were randomized and performed at 300 μm spacing such that

all diagonal indenters had the same orientation on the plane of interest. Each load was performed six times on the (010) axis and three times each on (110) and (011). Secondary electron (SE) and back-scattered electron (BSE) images of the indentation characteristics were obtained using a Hitachi SU-70 analytical Field Emission Scanning Electron Microscope (FESEM). The acceleration voltage range was 5 kV to 8 kV with a beam current of a few nano-amperes. The FESEM is ideally suited for characterizing micro-scale indentation tests because of its high magnification and three-dimensional resolution.

Raman spectroscopy measurements were obtained using a Renishaw inVia micro-Raman spectrometer at the Planetary and Space Science Centre (PASSC), University of New Brunswick. The fully automated Raman spectrometer is equipped with a 514.5 nm Ar^+ excitation laser. The spectrometer was used in backscattering geometry. The laser beam was focused through the microscope objectives (50x) down to a 2 μm area on the sample and the backscattered light was collected through the same objective. The spectra were recorded via a Peltier cooled CCD detector. The system is coupled with a high powered transmitted light microscope equipped with a precision motor-controlled X, Y, Z stage.

3. Experimental Results

3.1. Hardness Measurements

Vicker's hardness tests characterize a material's resistance to deformation, densification, displacement, and fracture, and is defined as [17]:

$$H_v = 1.854\frac{P}{d^2} \tag{1}$$

where P (kg) is the load and d (mm) is the average diagonal length of the indentation. Ultra-high resolution scanning electron microscope images were used to determine the indentation length and hardness values computed for the (010), (011), and (110) axes. Shown in Figure 2a are the mean hardness values, with bars denoting one standard deviation, for all axes. For all cases, H_v decreases with increasing load, ranging from 216 kg/mm^2 at 0.25 N to 91 kg/mm^2 at 4.91 N for (010) and from 122 kg/mm^2 at 0.98 N to 75 kg/mm^2 at 4.91 N for the other axes. The decreasing trend and plateau is consistent with previous investigations and is known as the "indentation size effect" [44–50]. Hardness values are higher than those presented by Taylor [18] of 60 kg/mm^2 at 0.49 N and are likely associated with his acknowledged uncertainty with the accuracy of his measurements. In his study, Taylor [18] used an optical microscope and had difficulty identifying the indentation edges in the translucent soft gypsum. Lower values of H_v on (011) and (110) are related to the increase in indentation length as a result of the increased depth of penetration when the tests were performed along cleavage planes.

Following methods outlined by Nix and Gao [51], the depth dependence of hardness can be characterized by:

$$\frac{H}{H_0} = \sqrt{1 + \frac{h^*}{h}} \tag{2}$$

where H is the hardness at a given depth, h, H_0 is the hardness limit at infinite depth and h^* is a characteristic length that depends on the shape of the indenter, shear modulus and H_0 [51]. Shown in Figure 2c is a plot of the $(H/H_0)^2$ against the inverse of the depth (determined from geometry of the tool and the measured indentation lengths) for each axis. The slope of the curve-fit line to this plot

is equal to h^*. Values of H_0=91 kg/mm^2 and h^*=15.0 μm are obtained for the (010) axis, H_0=77 kg/mm^2 and h^*=10.3 μm for (110), and H_0=75 kg/mm^2 and h^*=11.5 μm for (011).

3.2. Transmitted Light Microscopy

Despite numerous investigations on the effects of hardness upon fracture, there has been less attention given to the effects of cracking and their importance as a deformation component in indentation testing [36, 52]. Shown in Figure 3 are examples of transmitted light microscopy images for each load on (010). The indentation diagonals of the pyramid indenter are aligned with the vertical and horizontal orientation of all images. For brevity, only this axis is considered henceforth. For loads of 0.49 N and 0.98 N, subsurface cracking is shallow, as is suggested by the small depth of focusing below the indentations (Figure 3a and b). As the load is increased to 1.96 N (Figure 3c), more damage occurs in the vicinity of the indentation and surface concentric cracking and subsurface cracking along the (011) cleavage plane become more predominant. As the load is increased further to 2.94 N and to 4.91 N, subsurface cracking along the principal (110) cleavage plane (in Figure 3e) increases in both crack density and length. In addition, radial and concentric cracking accompany the dominant (110) subsurface cracking. Cracking along (110) occurs at 40° and 50° with respect the Vickers indenter edges, indicating that these cracks are initiated by the shearing of this cleavage plane. The median cracks developed at higher loads beneath the indentation enable the indenter to penetrate deeper, thereby producing larger indentations and reduced hardness [45].

3.3. Indentation Characteristics and Failure Modes

Backscattered electron (BSE) images on the (010) axis are shown in Figure 4. The use of backscatter electron microscopy is of value here as it is allows varying compositions, (e.g., cracks, densities, material compositions) to be differentiated. For example, materials with higher densities will appear darker in an BSE image. A highly fractured zone of fragments is observed on the sample's surface beneath the indenter for a load of 0.25 N (Figure 4a). The coalescence of concentric cracking and dislocations along (011) near the outer edge of the indentation results in the generation of blocky gypsum fragments. At this scale, surface cracking along (011) occurs more than along (110) (both are highlighted in Figure 4a). When the load is increased to 0.49 N, the surface beneath the indenter becomes smoother and darker (Figure 4b). The slightly darker portion indicates a different localized composition, which is likely more dense than its surrounding material. Radial cracking (labelled in Figure 4b) accompanies surface cracking along (011) and (110), as well as concentric cracking.

Shown in Figure 4c is an example of an indentation at a load of 0.98 N. Fragmentation in the vicinity of the indenter centre is observed at this load, as well as concentric cracking. Substantially larger surface cracks on (011) and (110) radiate at approximately 45° from the indenter edges, which are aligned with the vertical and horizontal axes of the images. These indicate shear stress failure in the soft gypsum material. When the load is increased further to 1.96 N, material at the outer edge of the indentation becomes raised above the original surface. This is known as pile-up (highlighted in Figure 4d), which contributes to supporting the load of the indenter [53]. Further increasing the load to 2.94 N (Figure 4e) results in an increase in pile-up. In addition, a ring of displacement material is

observed at the outer edge of the indentation for the 2.94 N load. This material is displaced upwards and out from the centre of the indenter during loading, as was noted by Tabor [17]. The surface of the indentation also becomes smoother. Further increasing the load to 4.91 N results in an increase in displacement material surrounding the indentation. The displaced material is a direct result of increased plastic flow of the material, leading to an increase in smoothness of the surface beneath the indenter.

The nature of the indentation surface is investigated further in Figure 5 for loads of 0.25 N, 0.49 N, 1.96 N, and 4.91 N. Cracking is commonly noted, but crack lengths and indentation features are often not typically characterized during micro-indentation experiments [54]. The visible crack density (i.e., the percentage of the surface that contain visible cracks) on the surface of the indentation zone decreases substantially as the load is increased. Imaging analysis was used to determine the total percentage of the indentation area that was associated with cracking (the dark area of the image). Results indicate that the indentation at 0.25 N is composed of 34 $\%$ crack density. Cracks are primarily aligned with the (011) axis. The crack density decreases to 17 $\%$ at 0.49 N, to 13 $\%$ at 1.96 N, and finally to 6 $\%$ at 4.91 N, where surface cracks have no preferable orientation. The decrease in crack density, and the increase in surface smoothness, is related to the increase in plastic flow of the surface material as the load is increased.

3.4. Raman Spectroscopy

Spatially distributed Raman spectroscopy measurements, beginning at the indentation centre and progressing away, are used to characterize the deformation in the gypsum crystal for loads of 0.98 N (Figures 6) and 4.91 N (Figures 7). These two loads are chosen because they characterize the transitional behaviour of the

gypsum in and near the indentation for both low and higher loads. Raman measurements along a line from the indentation centre to beyond the outer edge of the indentation are shown Figure 6a over wavelengths of 980 cm^{-1} to 1040 cm^{-1} for a load of 0.98 N. As reference, typical Raman spectra for undeformed gypsum is shown in Figure 6b. Gypsum has a dominant peak at 1008 cm^{-1} and minor intensity peaks at 415 cm^{-1}, 494 cm^{-1}, 671 cm^{-1}, 691 cm^{-1}, and 1136 cm^{-1}. Peaks found here are consistent with previous authors [55]. The dominant peak at 1008 cm^{-1} represents $\nu_1(SO_4)$, which is the first symmetric stretching mode of the sulfate ions in the gypsum. The locations of the Raman measurements from the plot in Figure 6(a) are shown in an optical microscope image in (c) and a scanning electron microscope image in (d). The Raman spectra in Figure 6a indicate that a single narrowband peak at 1008 cm^{-1} dominates the spectra at the centre of the indentation (location indicated by the circle in all sub-figures of Figure 6). The spectra becomes more broadband and a second peak at 1015 cm^{-1} begins to form near the edge of the indentation (location denoted by the hexagon). The Raman band at 1015 cm^{-1} increases and becomes dominant in the increasingly broadband spectra at the outer edge of the indentation (location denoted by the square). Raman spectra are plotted for Raman bands at 1008 cm^{-1} and 1015 cm^{-1} in Figure 6a for observing a micro-scale Raman shift. The peak at 1015 cm^{-1} corresponds to the water-reduced form of gypsum: hemihydrate, or bassanite ($CaSO_4 \cdot 0.5H_2O$) [1, 55]. A backscatter electron image of the material near the outer edge (hexagon and square locations) is shown in Figure 6e. The region is deformed and highly fractured. The peak intensity at 1015 cm^{-1} gradually reduces and the peak at 1008 cm^{-1} increases as moving away from the region of fractured gypsum (denoted by the square) until a single peak at 1008 cm^{-1}

dominates the narrowband spectra on the original surface of the gypsum crystal (location denoted by the star). This indicates that the hemihydrate phase is mainly distributed near the outer rim of the indentation.

Linear Raman mapping results from an indentation at 4.91 N is shown in Figure 7. Locations of the Raman measurements are shown in: (b) an optical microscope image and (c) a secondary electron image. The spectra at the centre location (denoted by a circle in all sub-figures) has an intense peak corresponding to 1008 cm^{-1}. The intensity of the peak increases in relative magnitude away from the centre to the outer edge of indentation. This is likely associated with an increase in the smoothness of the surface. The Raman band at 1008 cm^{-1} becomes broader, and a peak at 1015 cm^{-1} begins to form near the outer edge of the indentation (location denoted by the hexagon). The contribution to the Raman band at 1015 cm^{-1} further increases as measurements approach the outer edge of the indentation. In addition, a third Raman band at 1024 cm^{-1} appears at the outer edge (location of the final measurement and denoted by a star). The peak at 1024 cm^{-1} corresponds to the water-reduced form of gypsum: soluble anhydrite (γ-$CaSO_4$) [1, 55]. Raman spectra lines at 1008 cm^{-1}, 1015 cm^{-1} and 1024 cm^{-1} are plotted in Figure 7a for clarity. A broad Raman spectrum and secondary electron microscope image at the outer edge of the indentation (Figure 7d and e) indicate that that much of the material is highly deformed as a result of the plastic flow beneath the indenter, with some material being spheroidal in shape. The material comprises of hemihydrate and γ-$CaSO_4$ phases (Figure 7d), indicating that it primarily comprises water-reduced forms of gypsum.

3.5. Nanooscale Features of the Deformation of Gypsum

Nanoscale features of the deformation and fracture of gypsum are shown in Figure 8. Shown in Figure 8a is an area of deformation for the 0.25 N load. Most cracks are oval in shape, with cross-crack dimensions ranging from 35 nm to 188 nm. There is also evidence of plastic deformation in the form of necking across cracks. Necking likely occurred following the initial compression of the material and is brought on by frictional forces that are generated between surfaces and along grain boundaries during fracture [22, 29].

Shown in Figure 8b is a more clear example of spheroid formation at the outer edge of the indentation for a load of 4.91 N. The average diameter of the spheroid is approximately 130 to 180 nm. These are formed as a result of the large frictional forces at the micro-scale resulting in subsequent plastic deformation and heat generation of the material displaced beneath the indenter. Evidence of the formation of a string of gypsum spheroid is shown in Figure 8c. The string is approximately 152 nm in diameter and 2,470 nm in length. This feature was found located between adjacent fragmented surfaces in a location of highly fractured and melted gypsum Figure 4c. The string is composed of numerous spheroids, suggesting that the agglomeration of smaller spheroids was the mechanism behind its formation. Elevated temperatures needed to ”fuse” individual spheroids to form the cylindroid would need to be high enough that the material experienced localized melting (1400°C [56]). Lastly, shown in Figure 8d is a scanning electron microscope image of the smallest spheroid located near a dislocation. The spheroid is approximately 69 nm in diameter and the dislocation is approximately 38 nm across the centre. The spacing between dislocations is 133 nm. The smallest spheroid located is consistent with minimum values obtained by Osterwalder

et al. [57] who studied the nano-preparation of gypsum. More specifically, this is the limit at which fragments can form in gypsum, also known as the comminution limit.

4. Summary and Discussion

The deformation and fracture of gypsum under micro-indentation loading has been studied. Hardness values were found to decrease with increasing load, ranging from 216 kg/mm^2 at 0.25 N to 91 kg/mm^2 at 4.91 N for (010) and from 122 kg/mm^2 at 0.98 N to 75 kg/mm^2 at 4.91 N on (011), and (110). These values are larger than those presented by Taylor [18] of 60 kg/mm^2 at 0.49 N. Loads $<$0.25 N did not produce any significant indentations and full elastic recovery is assumed. Scanning electron microscopy allows indentation lengths to be measured more accurately in comparison to optical microscopy, especially when other effects such as pile-up [53] and cracking occur as a result of the indentation test. Lower values of H_v on (011) and (110) are related to the increased depth of penetration when the tests are performed, such that the indenter penetrated along cleavage planes. The observed inverse relationship between hardness and the load, or indentation size, is known as the "indentation size effect" and this has been observed and studied in other indentation experiments [44–50]. Size effects have also been observed in machining [58], uniaxial micro-scale compression experiments [59], thin foils in bending [60], copper wires in tension and torsion [61], and in thin-film mechanics [62–64].

Many associate the higher hardness, or strengths, with the saturation of dislocations [59] (i.e., no more dislocations can occur) in small volumes. This leads to non-uniform strains and associated large strain gradients [51, 65–70], thus pro-

moting local work-hardening. Gerberich et al. [65] proposed a theory in terms of a surface work and plastic volume work concept for depths below several hundred nanometers, while atomistic simulations [59] suggest that the "size effect" prevails at nano-scales regardless of strain gradients. Scanning electron microscopy indicates localized necking between cracks accompany the micro-scale deformation processes. This contributes to increased plastic flow and work hardening of the material as outlined by previous authors [51, 65–70]. Scanning electron microscopy also indicate localized material densification for lower loads.

Transmitted light microscopy reveals that shear-driven subsurface fracture along the other (110) cleavage plane increases in both crack density and length as the load is increased. The cracks beneath the indentation enable the indenter to penetrate deeper, thereby producing larger indentations and reduced hardness [45]. Coupled with an increase in shear-driven subsurface cracking was an increase in material flow beneath the indenter. This led to a decrease in crack density on the indentation surface as the load was increased, ranging from 34 $\%$ at 0.25 N to 6 $\%$ at 4.91 N. Material flow beneath the indenter results in the formation of spheroids. These were 130 to 180 nm in average size, with the smallest ones being 69 nm. These are formed as a result of the large frictional forces at the micro-scale and subsequent plastic deformation and heat generation of the material displaced beneath the indenter. Large inter-grain frictional forces also result in the formation and agglomeration of spheroids to form cylindroids. Temperatures needed to fuse individual spheroids together to form the cylindroid need to be high enough that the material experiences some melting (1400°C [56]).

Raman spectroscopy measurements presented here indicated dehydration of gypsum as a part of the deformation process under micro-indentation loading con-

ditions. Phase transformations through, for example, dehydration are important in efficiently processing minerals [71, 72]. Thermo-Raman analysis by Chang et al. [1] showed that the dehydration of gypsum ($CaSO_4{\cdot}2H_2O$) is a two step consecutive reaction into anhydrite, with hemihydrate ($CaSO_4{\cdot}0.5H_2O$) being the intermediate step. Within the temperature range of 118 to 142°C [1], gypsum transforms to hemihydrate, and then to anhydrate. Over this temperature range, water molecules are evaporated from the $CaSO_4{\cdot}2H_2O$ phase and concentrations of $CaSO_4{\cdot}0.5H_2O$ and $CaSO_4$ increase. Prasad et al. [55] noted an appreciable decrease in the peak intensity of the Raman measurements as a result of dehydration. This is to say that the peak intensity value at 1008 cm^{-1} is greater than the peak intensity value at 1015 cm^{-1} when the gypsum undergoes dehydration. The evaporated water molecules leave behind voids in the crystal structure, thereby allowing the material to deform easier. This contributed to the flow of surface material beneath the indenter and to the formation of spheroids observed in these experiments.

5. Conclusions

The micro-scale deformation and fracture of gypsum crystals from indentation loading has been examined. Simultaneous complex elastic, plastic, and fracture behaviour of gypsum exists for all loads. Results indicate that the hardness decreases with increasing load on all axes. Higher hardness values for lower loads is attributed to dislocation saturation and localized necking, which leads to work-hardening and densification. Transmitted light microscopy revealed that the decrease in hardness for increasing load was related to an increase in subsurface cracking along (110) and (011) cleavage planes, enabling the indenter to pene-

trate deeper. Coupled with an increase in subsurface cracking, was an increase in surface smoothness as a result of an increase in displaced material beneath the indenter (34 % crack density at 0.25 N in comparison to 6 % crack density at 4.91 N). Raman spectroscopy revealed that the material mainly comprises water-reduced forms of gypsum: hemihydrate and γ-$CaSO_4$. Local temperatures required for the dehydration of gypsum range from 118 to 142°C [1], indicating such temperatures are reached during plastic flow, and subsequent heat generation, beneath the indenter. Evidence of spheroid formation was also observed. Evaporated water leaves behind voids in the crystal structure and enables the gypsum to deform more easily. The formation of a string of spheroids indicates localized melting temperatures (1400°C [56]) are achieved between adjacent surfaces during fracture. The ease of transformation to allied water-reduced phases (hemihydrate and anhydrite) under nominally low temperatures conditions should be borne in mind for industrial processing applications.

6. Acknowledgments

The authors acknowledge the financial support of the Natural Sciences and Engineering Research Council of Canada, the Atlantic Innovation Fund, and the Atlantic Canada Opportunities Agency. We are also very grateful for the assistance from Vince Boardman of the Department of Mechanical Engineering and Karen Shea of the Planetary and Space Science Centre. This is Planetary and Space Science Centre contribution 76.

[1] H. Chang, P. J. Huang, S. Hou, Application of thermo-raman spectroscopy to study dehydration of $CaSO_4 2H_2O$ and $CaSO_4 0.5H_2O$, Materials Chemistry and Physics 58 (1) (1999) 12 – 19. doi:

10.1016/S0254-0584(98)00239-9.
URL http://www.sciencedirect.com/science/article/pii/S0254058498002399

[2] N. Mott, A theory of the fragmentation of shells and bombs, Technical Report AC4035, United Kingdom Ministry of Supply (May 1943).

[3] D. Shockey, D. Curran, L. Seaman, Fragmentation of rock under dynamic loads, International Journal of Rock Mechanics and Mining Sciences and Geomechanics Abstracts 11 (12) (1974) 250.

[4] D. Grady, Length scales and size distributions in dynamic fragmentation, International Journal of Fracture 163 (1–2) (2009) 85–99.

[5] M. A. Meyers, C. T. Aimone, Dynamic fracture (spalling) of metals, Progress in Materials Science 28 (1) (1983) 1 – 96.

[6] B. M. French, Traces of Catastrophe: A Handbook of Shock-Metamorphic Effects in Terrestrial Meteorite Impact Structures, LPI Contribution No. 954, Lunar and Planetary Institute, Houston, 1998.

[7] J. Aler, J. D. Mouza, M. Arnould, Measurement of the fragmentation efficiency of rock mass blasting and its mining applications, International Journal of Rock Mechanics and Mining Science and Geomechanics Abstracts 33 (2) (1996) 125 – 139.

[8] E. Strassburger, Ballistic testing of transparent armour ceramics, Journal of the European Ceramic Society 29 (2) (2009) 267 – 273, special Issue on Transparent Ceramics.

[9] M. L. Wilkins, Mechanics of penetration and perforation, International Journal of Engineering Science 16 (11) (1978) 793 – 807, special Issue: Penetration Mechanics.

[10] K. H. Zum-Gahr, Wear by hard particles, Tribology International 31 (10) (1998) 587 – 596.

[11] I. S. Buyuksagis, The effects of circular sawblade diamond segment characteristics on marble processing performance, Proceedings of the Institution of Mechanical Engineers, Part C: Journal of Mechanical Engineering Science 224 (8) (2010) 1559–1565. doi:10.1243/09544062JMES1950.

[12] J. D. Rodrigues, A. F. Pinto, D. R. da Costa, Tracing of decay profiles and evaluation of stone treatments by means of microdrilling techniques, Journal of Cultural Heritage 3 (2) (2002) 117 – 125. doi:DOI:10.1016/S1296-2074(02)01172-X.
URL http://www.sciencedirect.com/science/article/pii/S129620740201172X

[13] I. Inasaki, Grinding of hard and brittle materials, CIRP Annals - Manufacturing Technology 36 (2) (1987) 463 – 471.

[14] I. M. Hutchings, Ductile-brittle transitions and wear maps for the erosion and abrasion of brittle materials, Journal of Physics D: Applied Physics 25 (1A) (1992) A212.
URL http://stacks.iop.org/0022-3727/25/i=1A/a=033

[15] A. Evans, D. Marshall, Fundamentals of friction and of wear materials, American Society of Metals (1980) 439.

[16] R. Schuhmann, Principles of comminution, i. size distribution and surface calculations, AIME Tech. Publ (1189) (1940) 111 Mining Technology.

[17] D. Tabor, The Hardness of Metals, Clarendon Press, Oxford, 1951.

[18] E. W. Taylor, Correlation of the Mohs's scale of hardness with the Vickers's hardness numbers, Mineral. Mag (1949) 718 – 721.

[19] M. Sanad, E. Combe, A. Grant, The use of additives to improve the mechanical properties of gypsum products, Journal of Dental Research 61 (6) (1982) 808 – 810.

[20] A. Gendrin, N. Mangold, J.-P. Bibring, Y. Langevin, B. Gondet, F. Poulet, G. Bonello, C. Quantin, J. Mustard, R. Arvidson, S. LeMoulic, Sulfates in martian layered terrains: The omega/mars express view, Science 307 (5715) (2005) 1587–1591.

[21] C. Brookes, J. O'Neill, B. Redfern, Anisotropy in the hardness of single crystals, Proceedings of Royal Society A322 (1971) 73 82.

[22] W. F. Brace, Behavior of rock salt, limestone, and anhydrite during indentation, Journal Of Geophysical Research 65 (6) (1960) 1773–1788.

[23] D. Frew, M. Forrestal, W. Chen, A split hopkinson pressure bar technique to determine compressive stress-strain data for rock materials, Experimental Mechanics 41 (2001) 40–46.

[24] A. G. Evans, M. Linzer, Acoustic emission in brittle materials, Annual Review of Materials Science 7 (1) (1977) 179–208.

[25] D. Lockner, The role of acoustic emission in the study of rock fracture, International Journal of Rock Mechanics and Mining Sciences and Geomechanics Abstracts 30 (7) (1993) 883 – 899.

[26] T. Holmgeirsdottir, P. Thomas, Use of the D-762 shore hardness scleroscope for testing small rock volumes, International Journal of Rock Mechanics and Mining Sciences 35 (1) (1998) 85 – 92. doi:DOI:10.1016/S0148-9062(97)00317-3.
URL http://www.sciencedirect.com/science/article/pii/S0148906297003173

[27] H. Viles, A. Goudie, S. Grab, J. Lalley, The use of the schmidt hammer and equotip for rock hardness assessment in geomorphology and heritage science: a comparative analysis, Earth Surface Processes and Landforms 36 (3) (2011) 320–333. doi:10.1002/esp.2040.
URL http://dx.doi.org/10.1002/esp.2040

[28] K. K. Mathur, A. Needleman, V. Tvergaard, 3d analysis of failure modes in the charpy impact test, Modelling and Simulation in Materials Science and Engineering 2 (3A) (1994) 617.

[29] J. D. Hogan, J. G. Spray, R. J. Rogers, S. Boonsue, G. Vincent, M. Schneider, Micro-scale energy dissipation mechanisms during dynamic fracture in natural polyphase ceramic blocks, International Journal of Impact Engineering 38 (12) (2011) 931 – 939. doi:10.1016/j.ijimpeng.2011.06.004.
URL http://www.sciencedirect.com/science/article/pii/S0734743X11001035

[30] D. A. Shockey, A. Marchand, S. Skaggs, G. Cort, M. Burkett, R. Parker, Failure phenomenology of confined ceramic targets and impacting rods, International Journal of Impact Engineering 9 (3) (1990) 263 – 275.

[31] X. B. Li, D. A. Summers, G. Rupert, P. Santi, Experimental investigation on the breakage of hard rock by the pdc cutters with combined action modes, Tunnelling and Underground Space Technology 16 (2) (2001) 107 – 114. doi:DOI:10.1016/S0886-7798(01)00036-0.
URL http://www.sciencedirect.com/science/article/pii/S0886779801000360

[32] L. Chen, J. Labuz, Indentation of rock by wedge-shaped tools, International Journal of Rock Mechanics and Mining Sciences 43 (7) (2006) 1023 – 1033.

[33] B. R. Lawn, R. Wilshaw, Indentation fracture: principles and applications, Journal of Materials Science 10 (1975) 1049–1081.

[34] B. Mott, Micro-Indentation Hardness Testing, Butterworth, London, 1956.

[35] C. A. Brookes, R. P. Burnand, J. E. Morgan, Anisotropy and indentation creep in crystals with the rocksalt structure, Journal of Materials Science 10 (1975) 2171–2173.

[36] B. R. Lawn, A. G. Evans, D. B. Marshall, Elastic/plastic indentation damage in ceramics: The median/radial crack sysTEM, Journal of the American Ceramic Society 63 (9-10) (1980) 574–581. doi:10.1111/j.1151-2916.1980.tb10768.x.
URL http://dx.doi.org/10.1111/j.1151-2916.1980.tb10768.x

[37] Y. Kumashiro, A. Itoh, T. Kinoshita, M. Sobajima, The micro-Vickers hardness of TiC single crystals up to 1500C, Journal of Materials Science 12 (1977) 595–601.

[38] M. Darot, Y. Gueguen, Z. Benchemam, R. Gaboriaud, Ductile-brittle transition investigated by micro-indentation: results for quartz and olivine, Physics of The Earth and Planetary Interiors 40 (3) (1985) 180 – 186. doi:DOI:10.1016/0031-9201(85)90128-1.
URL http://www.sciencedirect.com/science/article/pii/0031920185901281

[39] C. C. Ferguson, G. E. Lloyd, R. J. Knipe, Fracture mechanics and deformation processes in natural quartz: a combined Vickers indentation, SEM, and TEM study, Canadian Journal of Earth Sciences 24 (3) (1987) 544–555.

[40] M. Chaudhri, C. Liangyi, The orientation of the hertzian cone crack in soda-lime glass formed by oblique dynamic and quasi-static loading with a hard sphere, Journal of Materials Science 24 (1989) 3441–3448.

[41] C. G. Knight, M. V. Swain, M. M. Chaudhri, Impact of small steel spheres on glass surfaces, Journal of Materials Science 12 (1977) 1573–1586.

[42] C. Kocer, R. E. Collins, Angle of hertzian cone cracks, Journal of the American Ceramic Society.

[43] B. R. Lawn, Hertzian fracture in single crystals with the diamond structure, Journal of Applied Physics 39 (10) (1968) 4828 –4836.

[44] M. V. Vliet, J. V. Mier, Effect of strain gradients on the size effect of concrete in uniaxial tension, International Journal of Fracture 95 (1999) 195–219,

10.1023/A:1018652302261.
URL http://dx.doi.org/10.1023/A:1018652302261

[45] G. D. Quinn, Indentation size effect for glasses: Yes, there is a fracture contribution, in: R. C. Bradt, D. Munz, M. Sakai, K. W. White (Eds.), Fracture Mechanics of Ceramics, Vol. 14 of Fracture Mechanics of Ceramics, Springer US, 2005, pp. 149–171.

[46] M. Atkinson, Further analysis of the size effect in indentation hardness tests of some metals, Journal of Materials Research 10 (11) (1995) 2908–2915.

[47] Q. Ma, D. R. Clarke, Size dependent hardness of silver single crystals, Journal of Materials Research 10 (4) (1995) 853–863.

[48] W. Poole, M. Ashby, N. Fleck, Micro-hardness of annealed and work-hardened copper polycrystals, Scripta Materialia 34 (4) (1996) 559–564.

[49] K. McElhaney, J. Vlassak, W. Nix, Determination of indenter tip geometry and indentation contact area for depth-sensing indentation experiments, Journal of Materials Research 13 (5) (1998) 1300–1306.

[50] S. Suresh, T.-G. Nieh, B. Choi, Nano-indentation of copper thin films on silicon substrates, Scripta Materialia 41 (9) (1999) 951–957.

[51] W. Nix, H. Gao, Indentation size effects in crystalline materials: A law for strain gradient plasticity, Journal of the Mechanics and Physics of Solids 46 (3) (1998) 411–425.

[52] J. T. Hagan, M. V. Swain, The origin of median and lateral cracks around

plastic indents in brittle materials, Journal of Physics D: Applied Physics 11 (15) (1978) 2091.

[53] P. Burnett, D. Rickerby, The scratch adhesion test: An elastic-plastic indentation analysis, Thin Solid Films 157 (2) (1988) 233 – 254.

[54] H. B. Abdelounis, K. Elleuch, R. Vargiolu, H. Zahouani, A. L. Bot, On the behaviour of obsidian under scratch test, Wear 266 (7-8) (2009) 621 – 626.

[55] P. S. R. Prasad, A. Pradhan, T. N. Gowd, In situ micro-raman investigation of dehydration mechanism in natural gypsum, Current Science 80 (9) (2001) 1203 – 1207.

[56] B. Ivanov, F. Langenhorst, A. Deutsch, U. Hornemann, Anhydrite eos and phase diagram in relation to shock decomposition, in: Lunar and Planetary Science XXXV: Impacts: Modeling and Observations, no. LPI-Contrib-1197, 2004.

[57] N. Osterwalder, S. Loher, R. Grass, T. Brunner, L. Limbach, S. Halim, W. Stark, Preparation of nano-gypsum from anhydrite nanoparticles: Strongly increased Vickers hardness and formation of calcium sulfate nanoneedles, Journal of Nanoparticle Research 9 (2007) 275–281.

[58] W. Gao, R. J. Hocken, J. A. Patten, J. Lovingood, Force measurement in a nanomachining instrument, Review of Scientific Instruments 71 (11) (Nov 2000) 4325.

[59] J. R. Greer, W. C. Oliver, W. D. Nix, Size dependence of mechanical properties of gold at the micron scale in the absence

of strain gradients, Acta Materialia 53 (6) (2005) 1821 – 1830. doi:10.1016/j.actamat.2004.12.031.
URL http://www.sciencedirect.com/science/article/pii/S1359645404007670

[60] J. S. A. Evans, A microbend test method for measuring the plasticity length scale, Acta Materialia 46 (14) (1998) 5109–5115.

[61] M. G. A. M. H. J. Fleck, N.A., Strain gradient plasticity: Theory and experiment, Acta Metallurgica Et Materialia 42 (2) (1994) 475–487, cited By (since 1996) 1063.
URL http://www.scopus.com/inward/record.url?eid=2-s2.0-0028370983&partnerID=40&md5=238ba9ab055f8beb3ecf324411d734e1

[62] J. Matthews, A. Blakeslee, Defects in epitaxial multilayers. i. misfit dislocations, Journal of Crystal Growth 27 (C) (1974) 118–125.

[63] W. Nix, Mechanical properties of thin films, Metallurgical Transactions A 20 (11) (1989) 2217–2245.

[64] L. Freund, Stability of a dislocation threading a strained layer on a substrate., Journal of Applied Mechanics, Transactions ASME 54 (3) (1987) 553–557.

[65] W. Gerberich, N. Tymiak, J. Grunlan, M. HorsTEMeyer, M. Baskes, Interpretations of indentation size effects, Journal of Applied Mechanics, Transactions ASME 69 (4) (2002) 433–442.

[66] H. Gao, Y.-Y. Huang, W. Nix, Modeling plasticity at the micrometer scale, Naturwissenschaften 86 (11) (1999) 507–515.

[67] Huang, M.-K. Ting, B.-S. Hsu, J.-S. Tsai, Demonstration of reserved anterior pituitary function among patients with amenorrhea after postpartum hemorrhage, Gynecological Endocrinology 14 (2) (2000) 99–104.

[68] Huang, Z. Xue, H. Gao, W. Nix, Z. Xia, A study of microindentation hardness tests by mechanism-based strain gradient plasticity, Journal of Materials Research 15 (8) (2000) 1786–1796.

[69] Y.-Y. Huang, J. Chen, T. Guo, L. Zhang, K. Hwang, Analytic and numerical studies on mode I and mode II fracture in elastic-plastic materials with strain gradient effects, International Journal of Fracture 100 (1) (1999) 1–27.

[70] N. Fleck, J. Hutchinson, A phenomenological theory for strain gradient effects in plasticity, Journal of the Mechanics and Physics of Solids 41 (12) (1993) 1825 – 1857. doi:10.1016/0022-5096(93)90072-N.
URL http://www.sciencedirect.com/science/article/pii/002250969390072N

[71] H. Lutz, A cyclic amp-dependent phosphoylation of spectrin dimer, FEBS Letters 169 (2) (1984) 323–329.

[72] H. Lutz, W. Eckers, H. Christian, B. Engelen, Hydrates of barium hydroxide. preparation, thermal decomposition and x-ray data, Thermochimica Acta 44 (3) (1981) 337 – 343.

List of Figures

Fig1. Gypsum crystal photo and schematic with principal axes

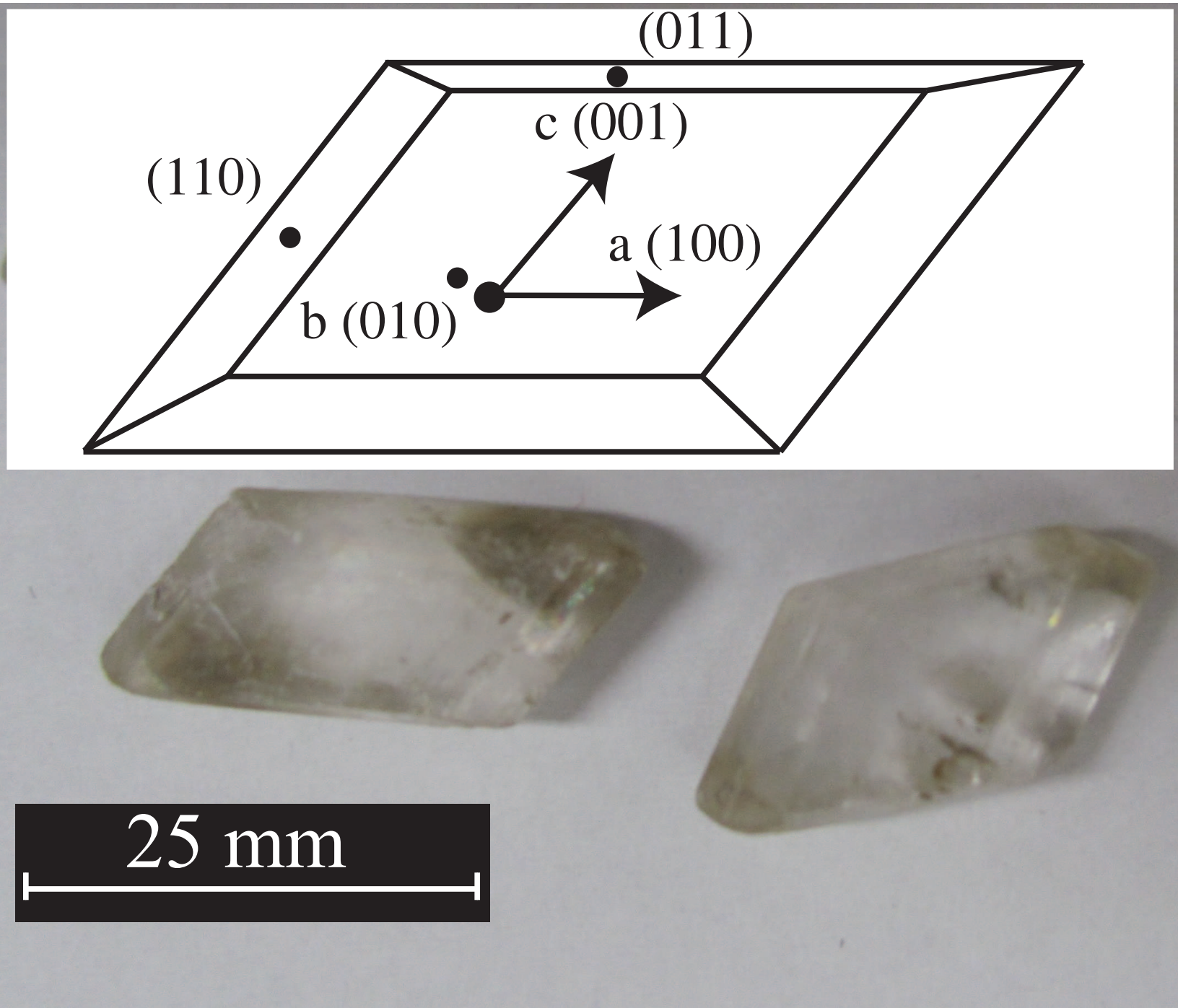

Fig2 (a) Mean hardness values and (b) Nix and Gao depth-Hv model

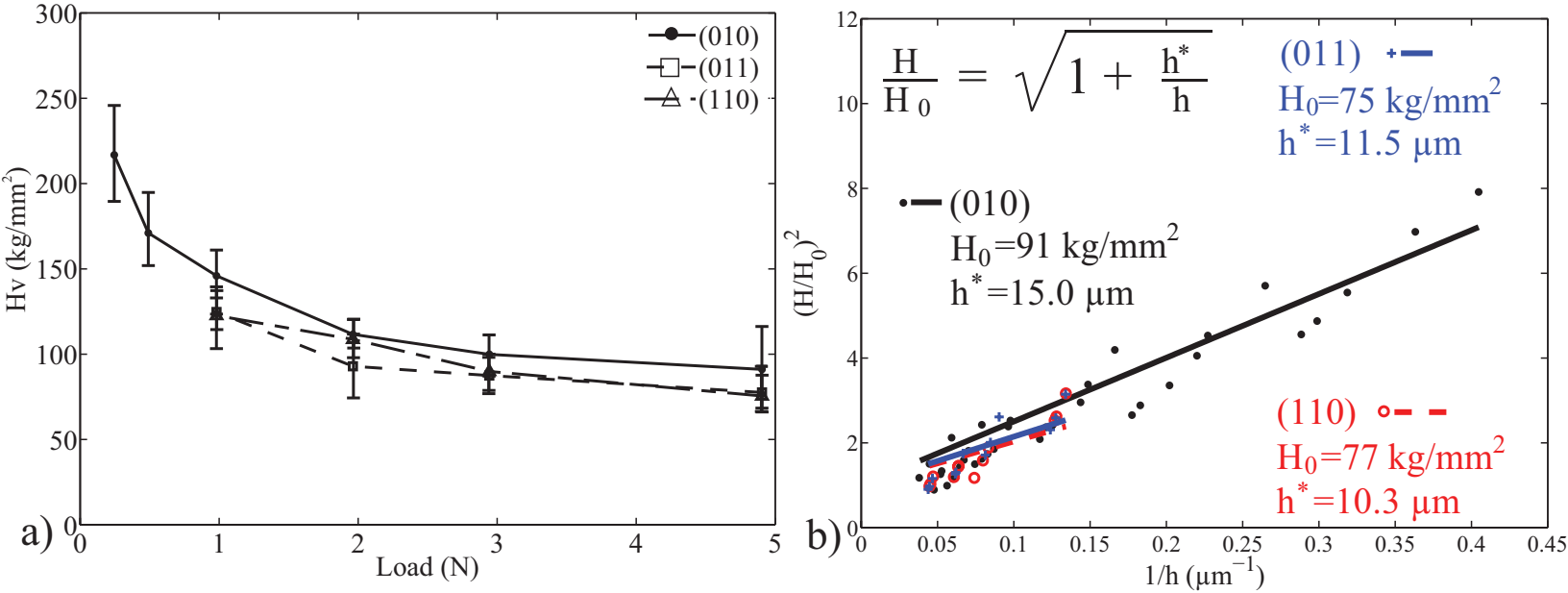

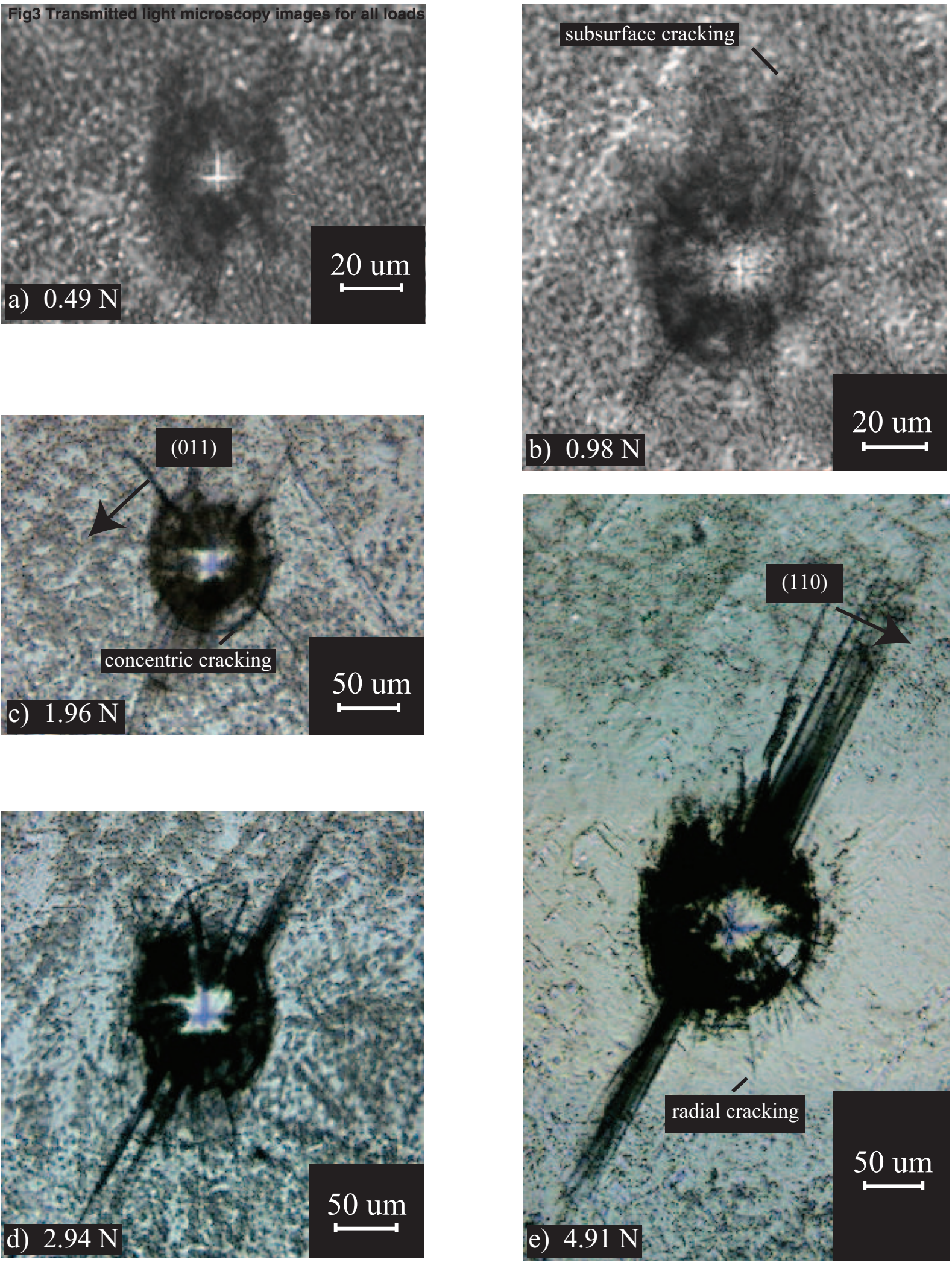
Fig3 Transmitted light microscopy images for all loads
20 um
a) 0.49 N
subsurface cracking
20 um
b) 0.98 N
(011)
concentric cracking
50 um
c) 1.96 N
50 um
d) 2.94 N
(110)
radial cracking
50 um
e) 4.91 N

Fig. Backscatter electron microscope images on (010)

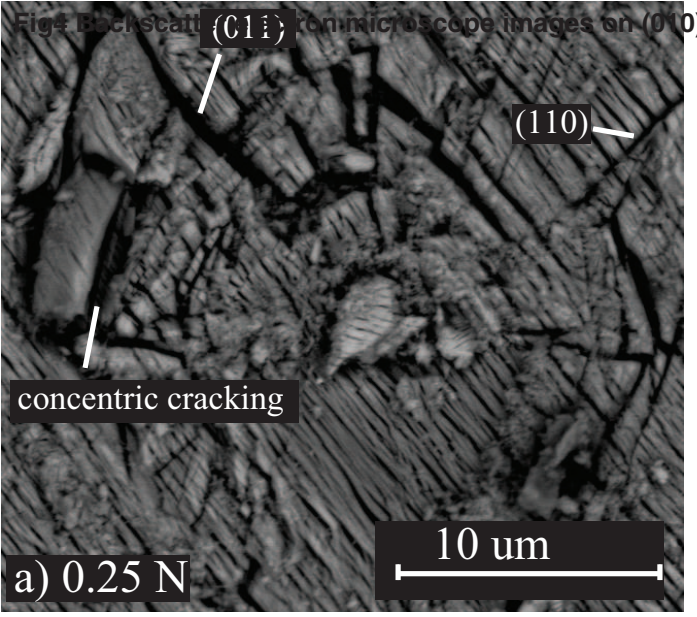

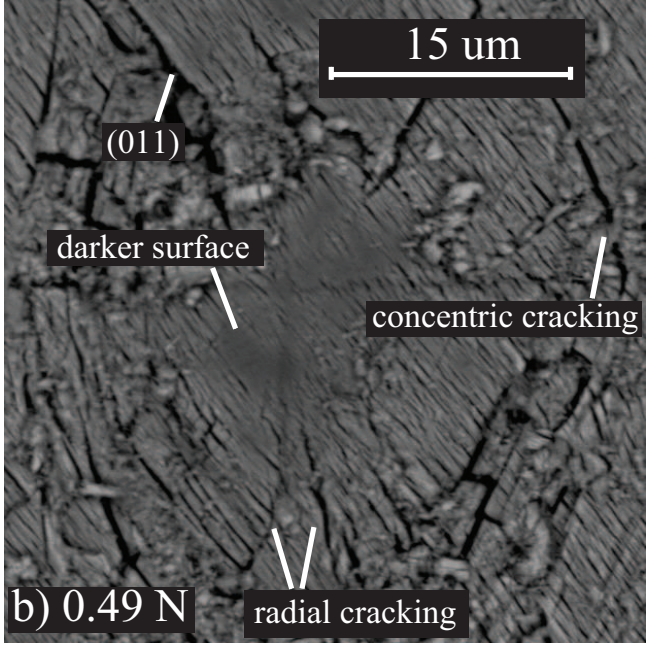

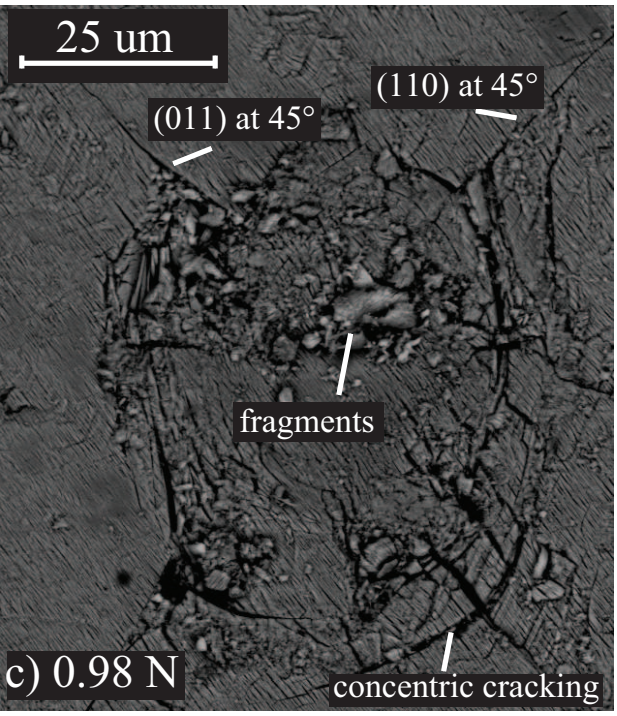

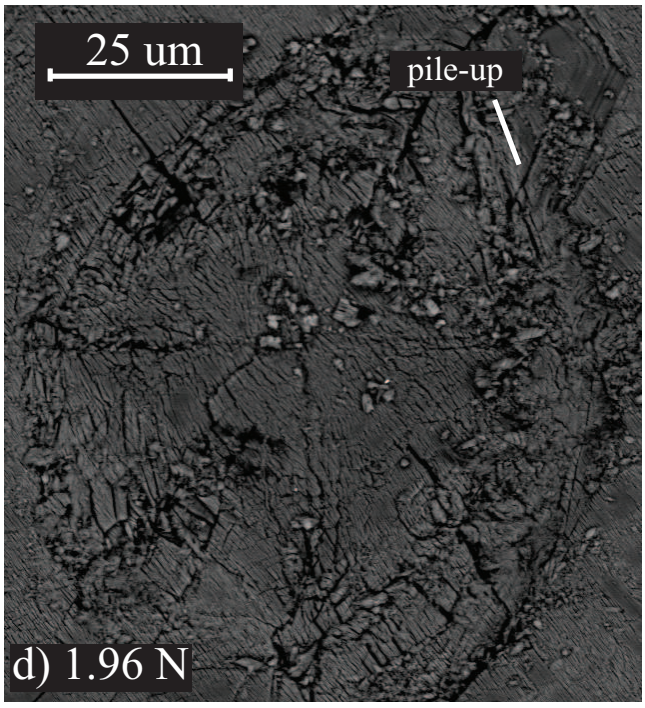

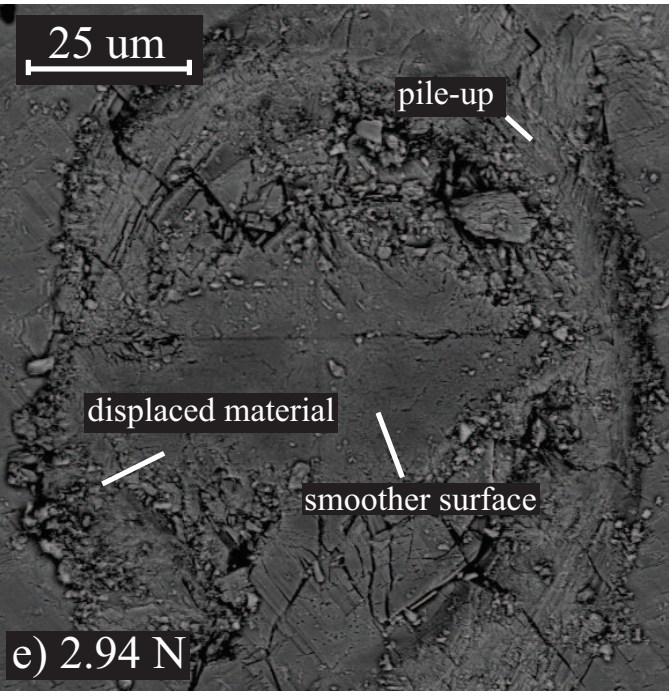

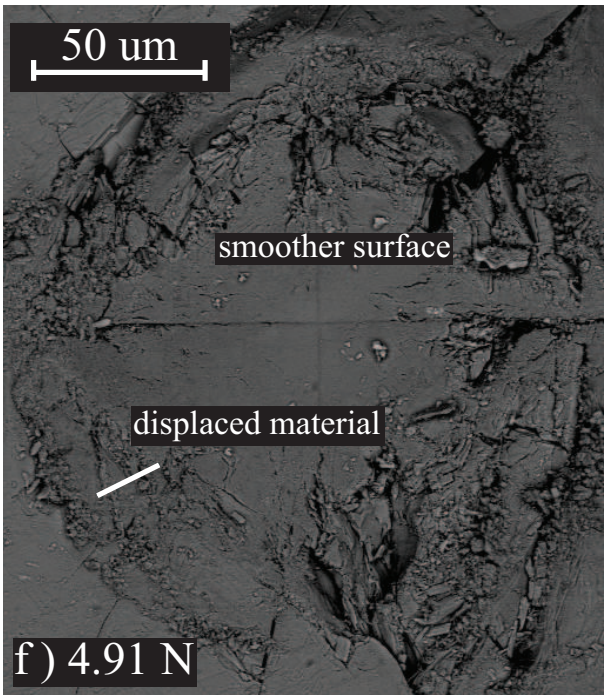

Fig5 SEM images of indentation central region

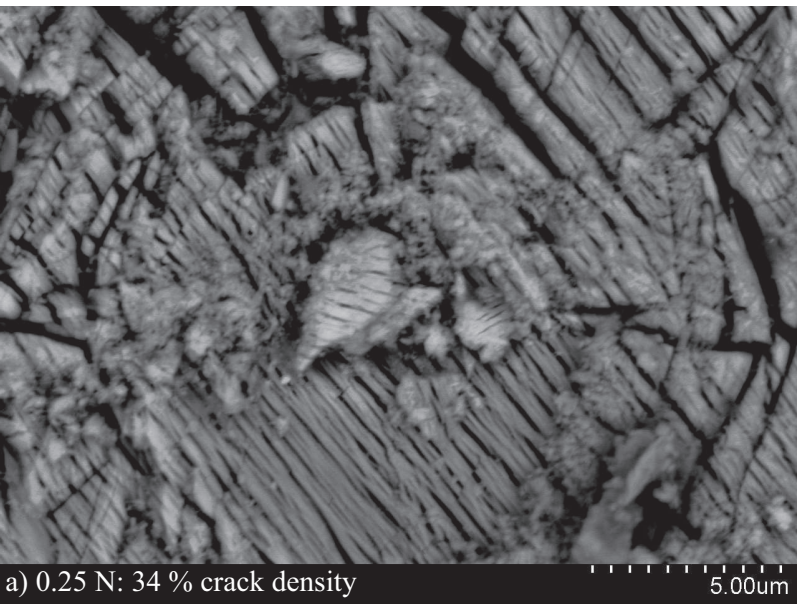

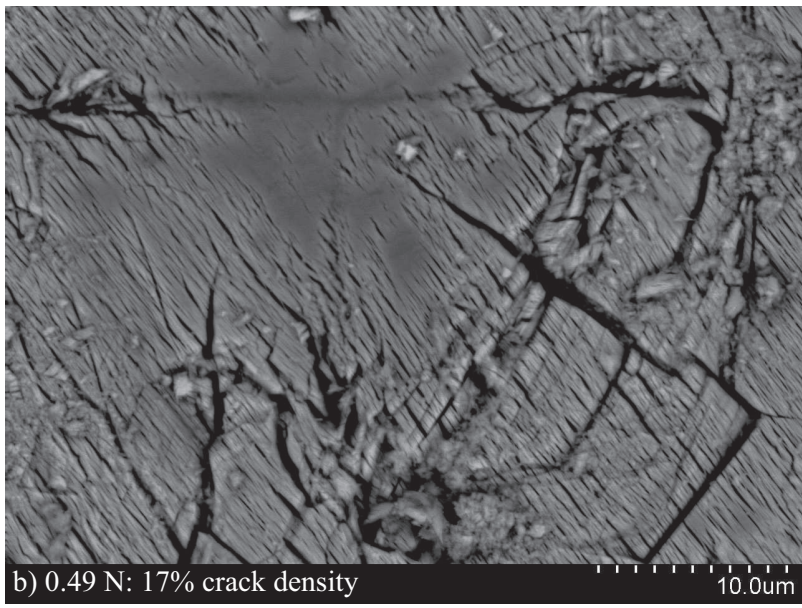

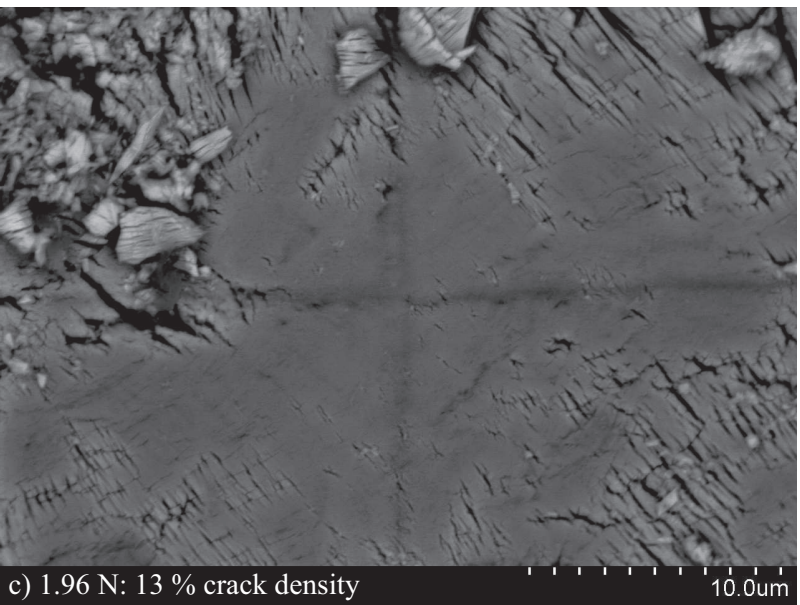

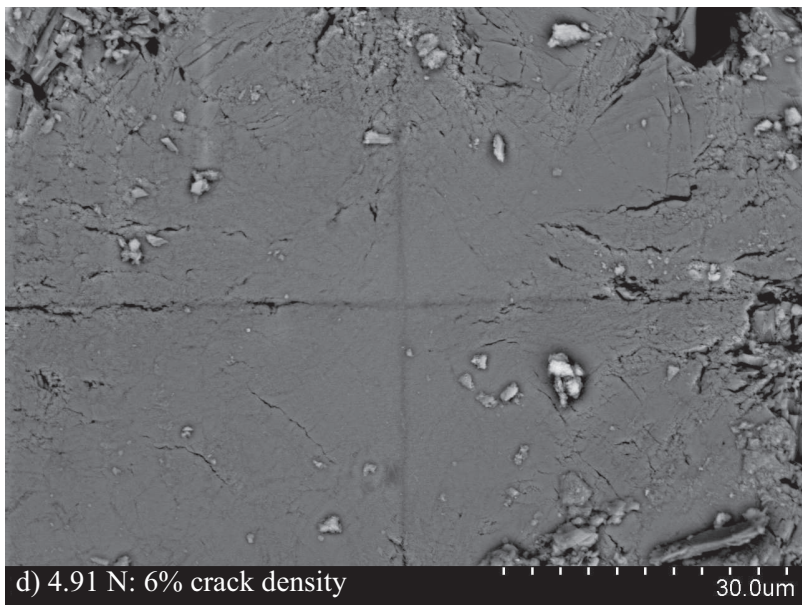

Fig6 Raman measurements for 0.98 N

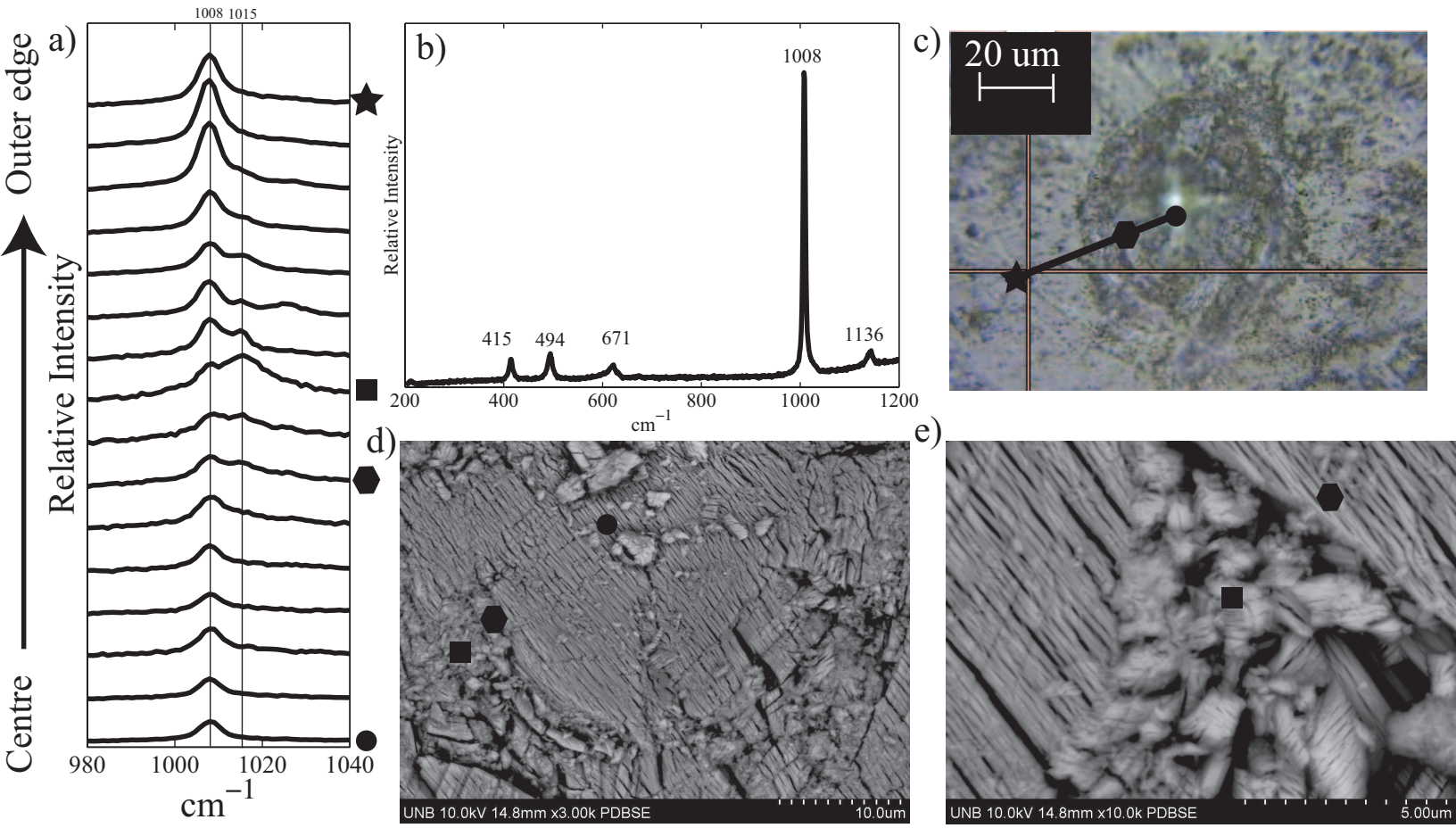

Fig7 Raman measurements for 4.91 N

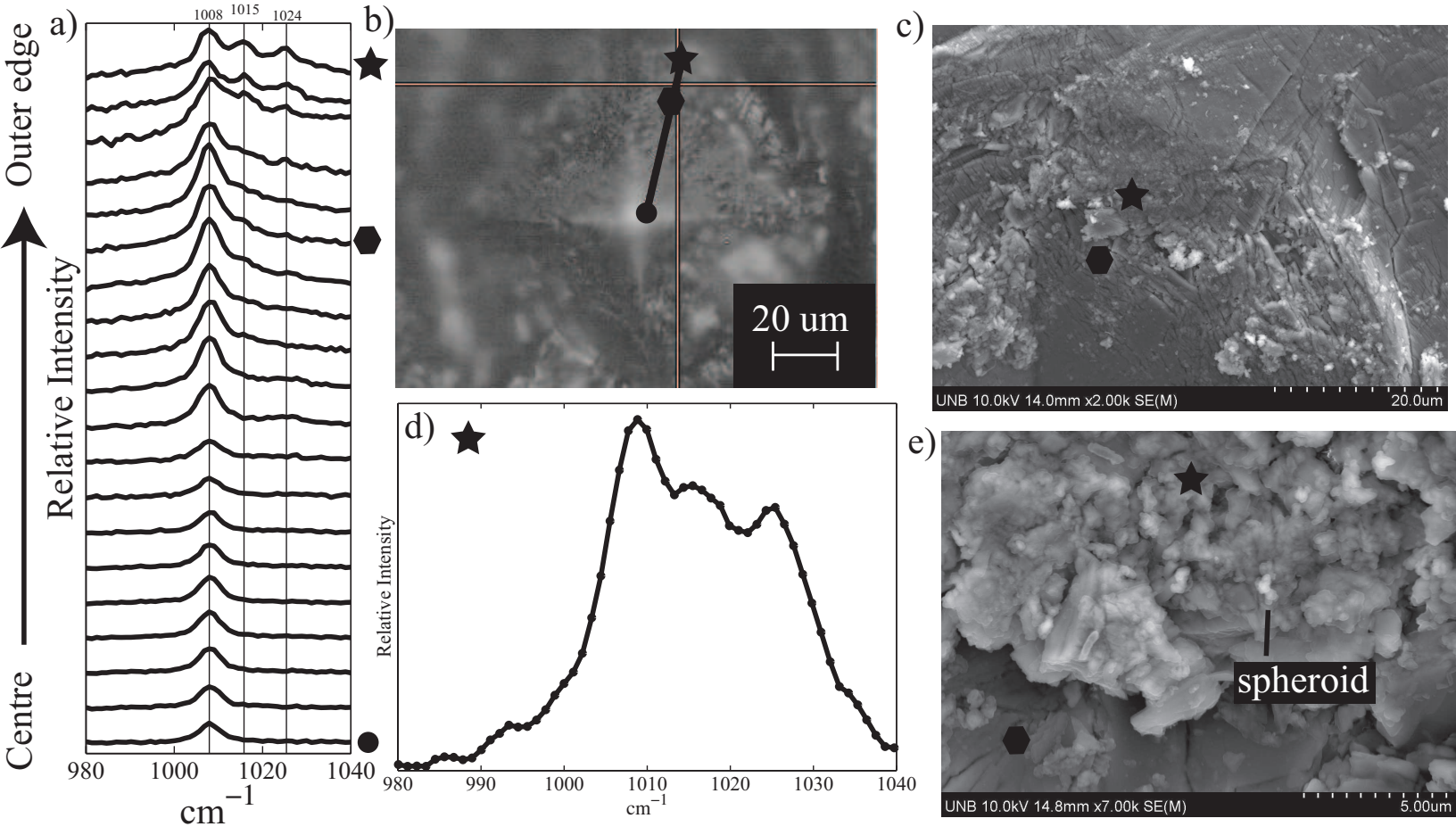

Fig8 Nanoscale features